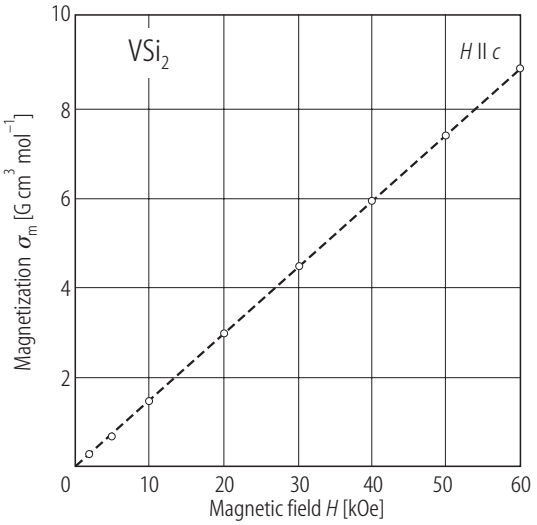

Fig. 3. VSi_2. Dependence of magnetization σ_m on an applied magnetic field H parallel to the c axis at 4 K [93G2].

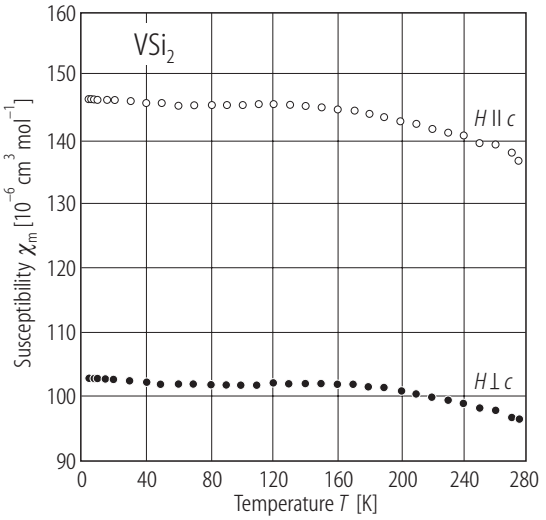

Fig. 4. VSi_2. Temperature dependence of the molar magnetic susceptibility χ_m in a magnetic field parallel or perpendicular to the c axis [93G2].

1.5.4.3 Cr alloys and compounds

Most of the work in the last decade is related to the spin-density-wave antiferromagnetism of Cr. Dilute alloys of Cr have been investigated extensively, as reviewed by [94F1]. See also subsect. 1.1.1.3 in LB III/19A.

Survey

	Composition x	Properties	Figure	Table
$Cr_{1-x}Si_x$	0.0142...0.00343	thermal expansion $\Delta l/l(T)$	5	
	0.005	$c_{ij}(T)$	6	
	0.0185	$\rho(T;p)$	7	
	0.0085	$Q(T)$	8	
	0...0.0046	x-T magnetic phase diagram	9	
$CrSi_2$		$\chi_m(T^{-1})$	10	3
$CrGe_{1-x}Si_x$	0...0.15	$\chi_g(T)$	11	
$Cr_{1-x}Ge_x$	0...0.0105	x-T magnetic phase diagram	12	
	0.0051...0.0089	p-T magnetic phase diagram	13	
$Cr_{1-x}Sn_x$	0.0007...0.0118	Mössbauer spectra	14	
	0...0.030	x-T magnetic phase diagram	15	
$(Cr_{0.987}Si_{0.013})_{1-x}V_x$	0...0.0031	thermal expansion $\Delta l/l(T)$	16	
$(Cr_{0.987}Si_{0.013})_{1-x}Mn_x$	0.0017…0.0232	thermal expansion $\Delta l/l(T)$	17	

	Composition x	Properties	Figure	Table
$(Cr_{0.987}Si_{0.013})_{1-x}(V,Mn)_x$	0...0.006 (V), 0...0.0073 (Mn)	x-*T* magnetic phase diagram	18	
$Cr_{0.79}Mn_{0.21}Ge$		$\sigma(T)$	19	
$Cr_{1-x}Mn_xGe$	0.1...0.6	x-*T* magnetic phase diagram	20	

Table 3. Supplement to Table 4 in LB III/19C, subsect. 1.5.4.3. Magnetic and related properties of $CrSi_2$ [90O1].

	$CrSi_2$
Crystal structure	hexagonal, C40
a [Å]	4.242
c [Å]	6.342
Magnetism	dia

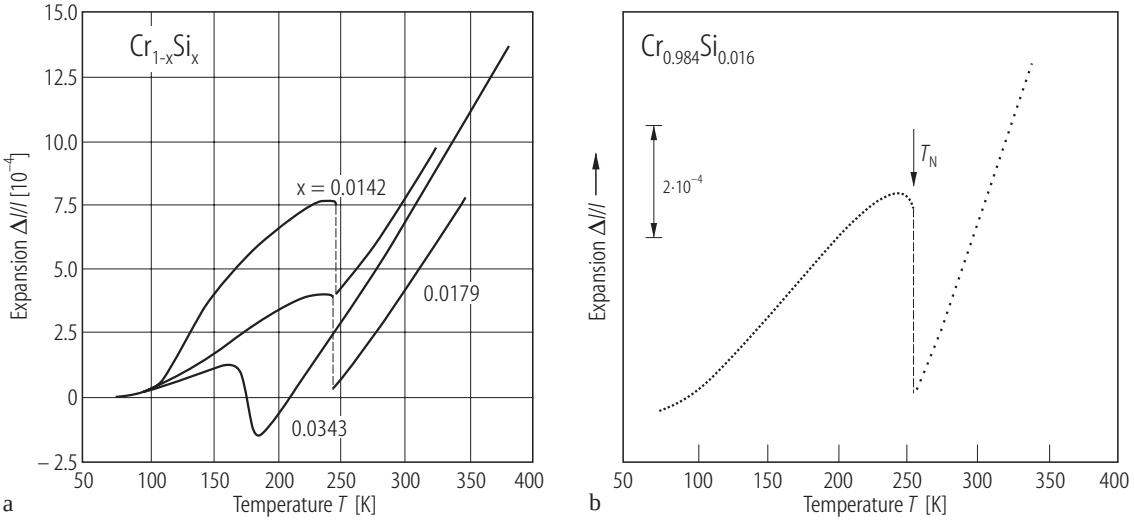

Fig. 5. $Cr_{1-x}Si_x$. Temperature dependence of thermal expansion $\Delta l/l$ (**a**) polycrystals [88A1], (**b**) along the [110] direction of a single crystal with x = 0.016 [93L1].

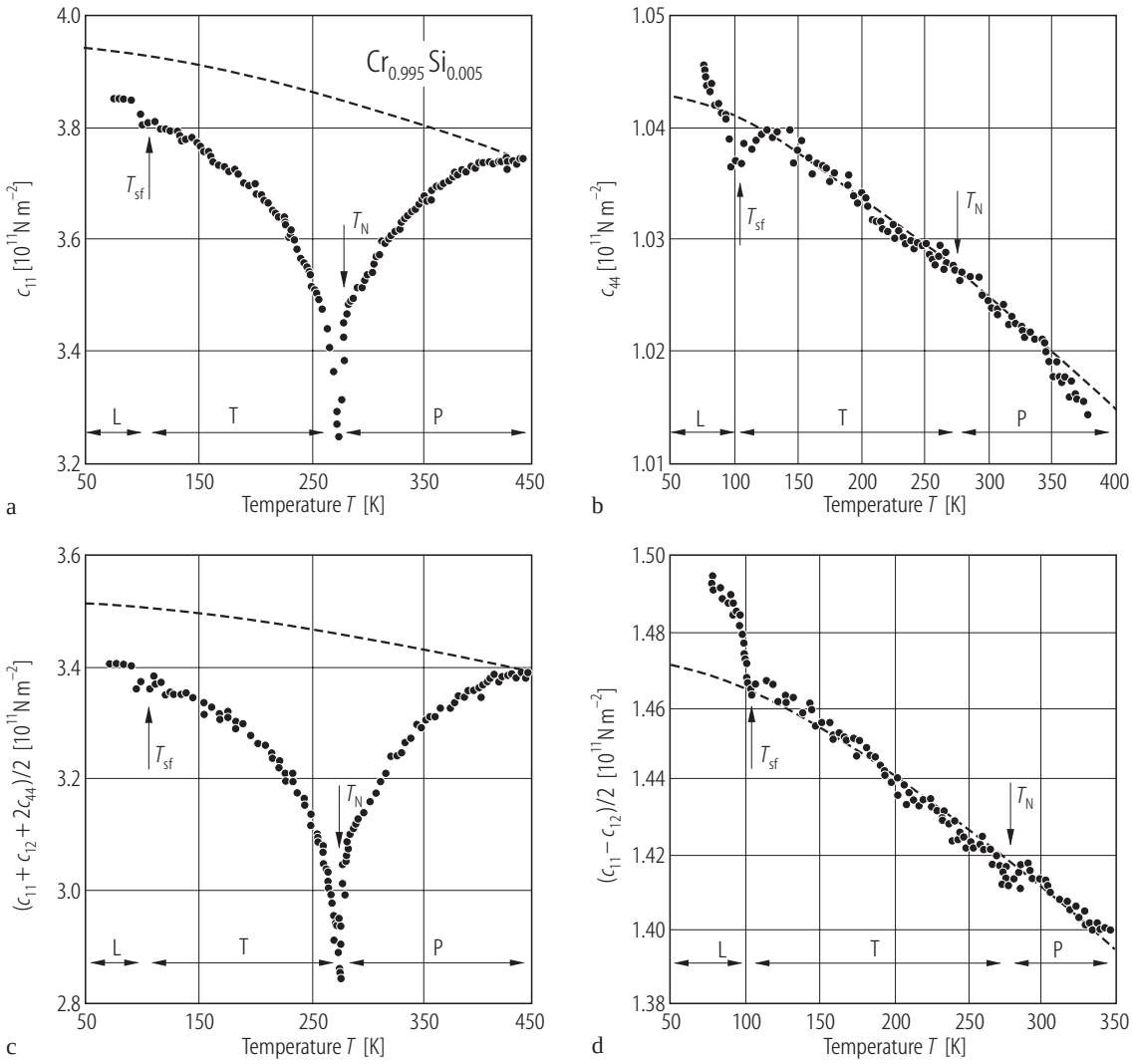

Fig. 6. $Cr_{0.995}Si_{0.005}$. Temperature dependence of the elastic constants. (**a**) c_{11}, (**b**) c_{44}, (**c**) $(c_{11}+c_{12}+2c_{44})/2$, (**d**) $(c_{11}-c_{12})/2$. P: paramagnetic state; T and L: transverse and longitudinal incommensurate spin wave states, respectively. The broken curves show the estimated non-magnetic behaviour based on the curve for Cr–5 at% V [93A2].

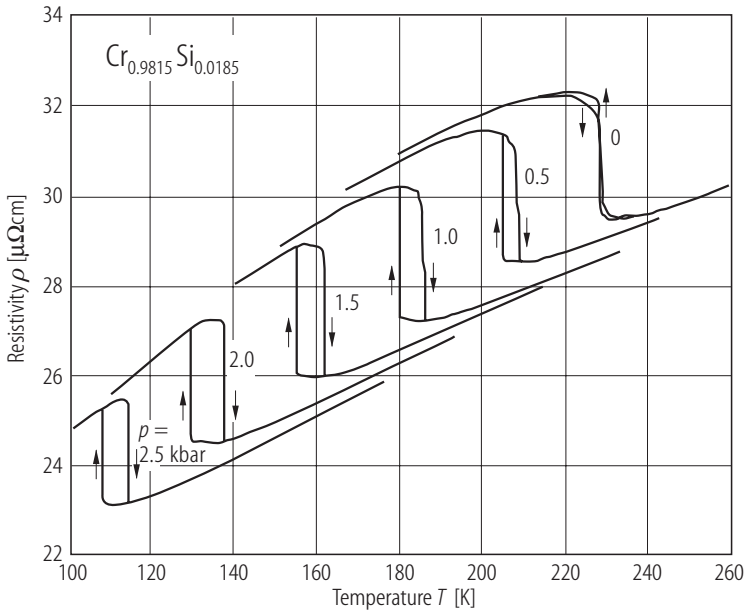

Fig. 7. $Cr_{0.9815}Si_{0.0185}$. Temperature dependence of the electrical resistivity ρ under various pressures p [91H1].

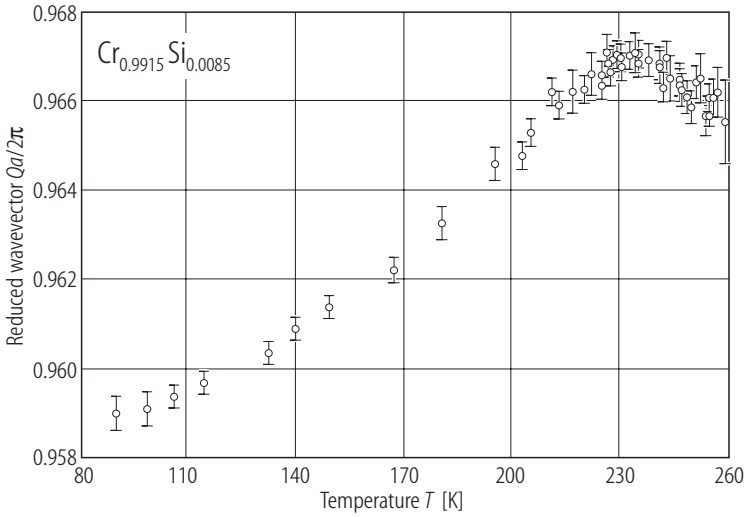

Fig. 8. $Cr_{0.9915}Si_{0.0085}$. Temperature evolution of the magnitude of the spin density wavevector Q in units of $2\pi/a$ [86M1].

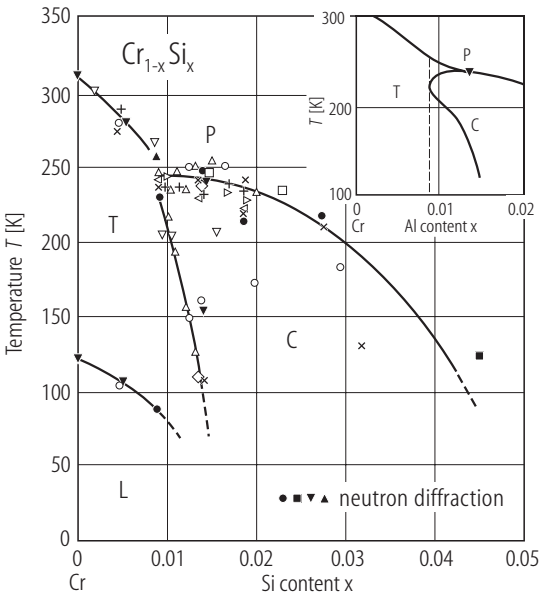

Fig. 9. $Cr_{1-x}Si_x$. Magnetic phase diagram in the temperature vs. composition plane. Symbols P, C, T and L indicate the paramagnetic (P) state and the commensurate (C), incommensurate transverse (T) and incommensurate longitudinal (L) spin density wave states. Solid symbols: neutron diffraction, the upright triangle corresponding to Fig. 8 [86M1]; other symbols: ρ, χ, C , B, α. Different symbols correspond to different authors. The inset shows the phase diagram around the triple point, with a re-entrant C phase, as inferred from the data shown in Fig. 8. The dashed line corresponds to the concentration x = 0.0085 [93F1, 94F1].

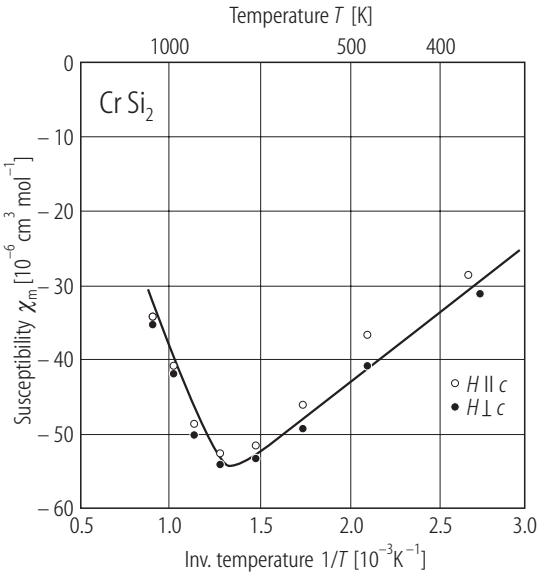

Fig. 10. $CrSi_2$. Molar magnetic susceptibility χ_m vs. inverse temperature T^{-1}, for the measuring field $H \parallel$ and $\perp$ to the c axis [90O1].

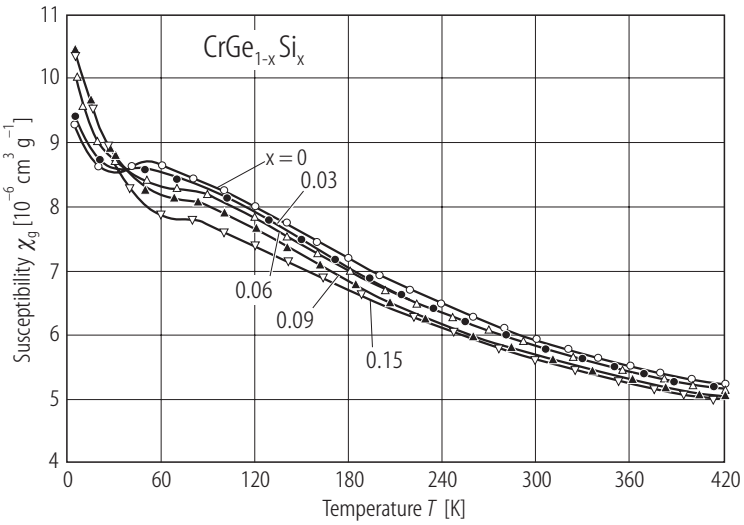

Fig. 11. $CrGe_{1-x}Si_x$. Temperature dependence of magnetic mass susceptibility χ_g [86S1].

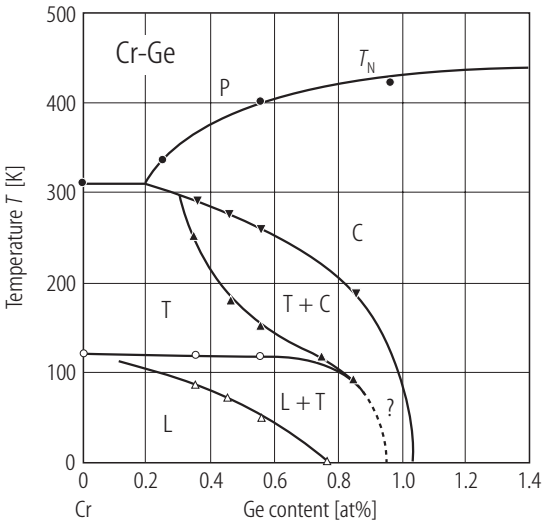

Fig. 12. Cr–Ge. Magnetic phase diagram in temperature vs. composition plane determined from neutron diffraction results [92B1]. P: paramagnetic; C: commensurate; T and L: transverse and longitudinal incommensurate states.

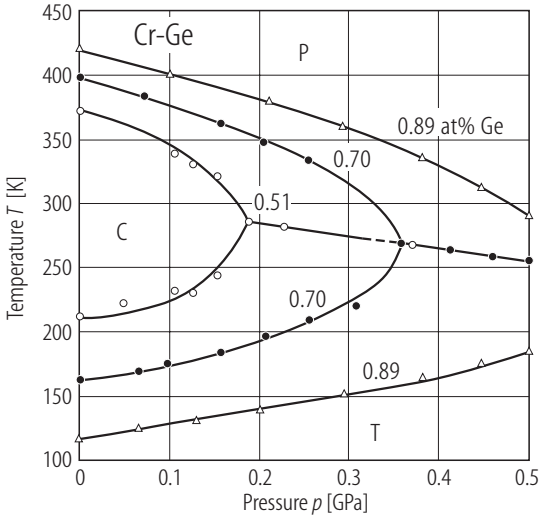

Fig. 13. Cr–Ge. Magnetic phase diagram in temperature vs. pressure plane determined from electrical resistivity. P: paramagnetic; C: commensurate spin density wave; T: incommensurate transverse spin density wave [94F1, 86V1].

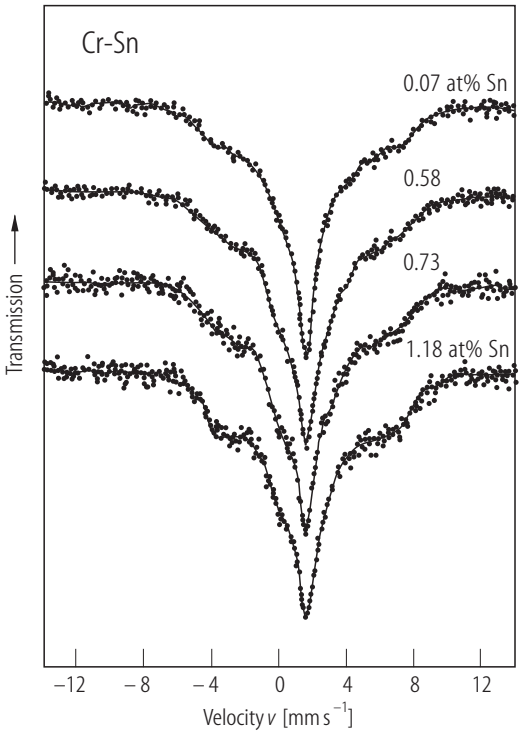

Fig. 14. Cr–Sn. Mössbauer spectra of ^{119}Sn at room temperature. The lines due to undissolved βSn have been subtracted [93D1].

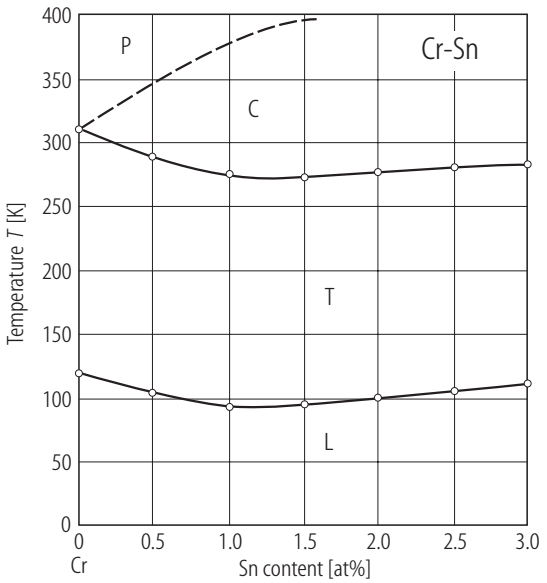

Fig. 15. Cr–Sn. Magnetic phase diagram in temperature vs. composition plane determined from neutron diffraction [85O1]. The Néel temperature (dashed curve) is based on the electrical resistance measurements by [72F2]. P: paramagnetic; C: commensurate spin density wave; T and L: transverse and longitudinal incommensurate spin density waves, respectively.

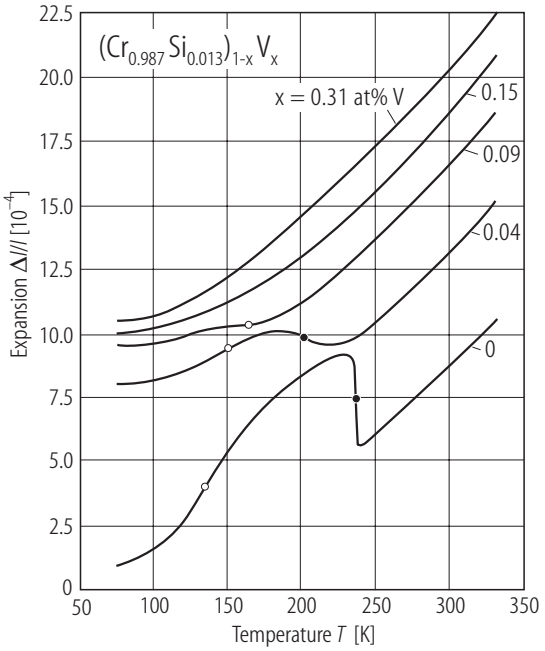

Fig. 16. $(Cr_{0.987}Si_{0.013})_{1-x}V_x$. Temperature dependence of thermal expansion $\Delta l/l$. Solid circles: Néel temperature; open circles: incommensurate - commensurate spin-density-wave phase transition temperature [93G1].

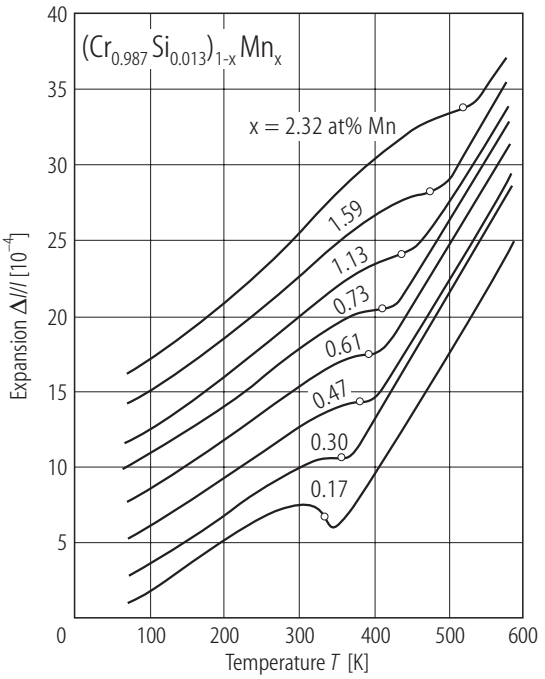

Fig. 17. $(Cr_{0.987}Si_{0.013})_{1-x}Mn_x$. Temperature dependence of thermal expansion $\Delta l/l$. Open circles on the curves show the Néel temperature [93G1].

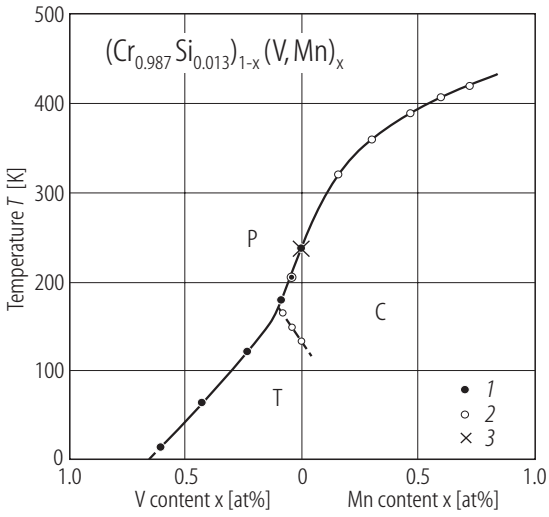

Fig. 18. $(Cr_{0.987}Si_{0.013})_{1-x}(V \text{ or } Mn)_x$. Magnetic phase diagram in x-T plane, with the phase boundaries obtained from: (*1*) ρ (T) [86G1]; (*2*) and (*3*) thermal expansion (Figs. 16 and 17), (*3*) showing first-order transition [93F1]. P: paramagnetic state, C and T: commensurate and transverse incommensurate spin density wave states, respectively.

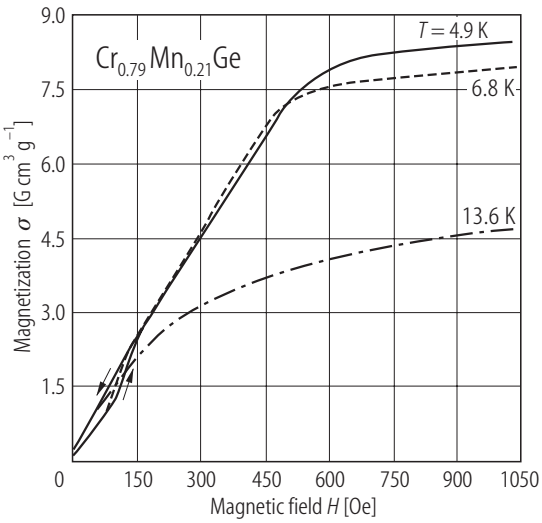

Fig. 19. $Cr_{0.79}Mn_{0.21}Ge$. Dependence of mass magnetization σ on applied magnetic field H at various temperatures [87S1].

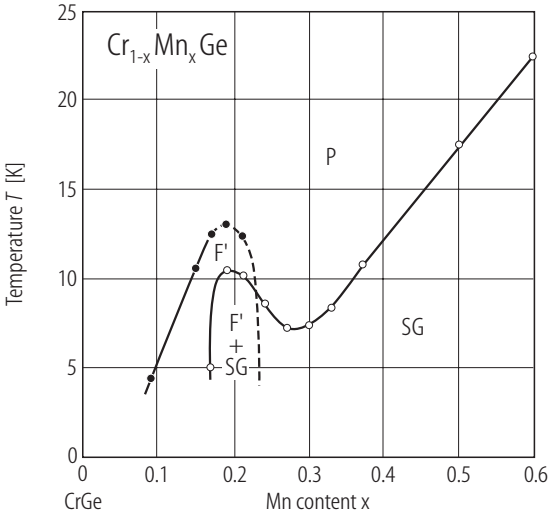

Fig. 20. $Cr_{1-x}Mn_xGe$. Magnetic phase diagram in temperature vs. composition plane proposed on the basis of detailed magnetic measurements [88S1]. P: paramagnetic state; SG: spin glass state; F': ferromagnetic or helical magnetic (for x = 0.19) state [94S1].

1.5.4.4 Mn alloys and compounds

Compounds of Mn with Si, Ge or Sn exhibit a variety of types of magnetic ordering. In particular, Mn_3Sn, a triangular antiferromagnet with uncompensated remanent magnetic moment, has got much attention since [82T1, 82T2]. The sample dependence of the magnetic properties of this compound suggests a delicate energy balance. It should be mentioned also that the magnetism of the most Si-rich compound $MnSi_{1.75-x}$ seems to be left unclarified as a consequence of the sensitivity of the crystal structure to the preparation conditions. Note also that the composition $Mn_{11}Si_{19}$ belongs to this group. According to [86Y3] it has a "chimney-ladder" structure, in which the Mn atoms form a tetragonal arrangement (chimney) with lattice parameters a = 5.52 Å and c_{Mn} = 4.37 Å while the Si atoms occupy interstices of the Mn sublattice, forming a coupled helical arrangement (ladder) with a period c_{Si} around 4 c_{Mn} [86Y3]. The change of the ratio c_{Si}/c_{Mn} with x and temperature leads to a variety of long-period or rather incommensurate structures, which makes it difficult to understand the physical properties of this and also of the related ternary compounds.

Survey

Composition x	Properties	Figure	Table
$Mn_{0.912}Si_{0.088}$	$H_{hyp}(T)$	21	
Mn_3Si	$\omega(q)$	22	
$Mn_{2.8}Fe_{0.2}Si$	$\omega(q)$	23	
Mn_5Si_3	magnetic structure	24	4
	$\sigma(H;T)$	25	
MnSi	$T_1^{-1}(T)$ for muon, ^{55}Mn	26	
	$\rho(T;p)$	27	
	neutron paramagnetic scattering $(\hbar\omega,Q;T)$	28	